Engineering Solid Mechanics 14 (2026) 173-186

Contents lists available at GrowingScience

Engineering Solid Mechanics

homepage: www.GrowingScience.com/esm

Modeling the effect of matric suction on a spherical particle mixture using discrete element method in PFC 3D

José Rico Anjarasoaherilalaina[a,b*], Bertrand François[c] and Luc Rakotondrajaona[a]

[a]*Ecole du Génie Civil, Institut Supérieur de Technologie d'Antananarivo, B.P : 8122 - Antananarivo 101, Madagascar*
[b]*Ingénierie et Géosciences (INGE), Université d'Antananarivo, Campus Universitaire Ankatso, Antananarivo 101, Madagascar*
[c]*Department of Urban and Environmental Engineering (UEE), University of Liège, Liège, Belgium*

ARTICLEINFO

Article history:
Received 10 January 2026
Accepted 22 February 2026
Available online
22 February 2026

Keywords:
Suction
Discrete element method
Compressive strength
Contact model

ABSTRACT

Unsaturated soils and granular materials play a pivotal role in geotechnical and environmental engineering, with water under tension markedly influencing their mechanical behavior, particularly strength and deformation. To elucidate the impact of matric suction on the macroscopic mechanical response, this study presents a modeling approach for capillary interactions between spherical particles in a partially saturated medium using the Discrete Element Method (DEM). The PFC3D software is employed to calibrate mesoscale interparticle contact parameters to replicate uniaxial compression tests performed on a reference material under saturated conditions. Suction effects are incorporated via an intergranular contact force based on the Hill contact model, which considers matric suction magnitude, particle radius, and interparticle spacing. Numerical results demonstrate that suction can be realistically represented by an adhesion force at particle contacts. The model is further extended to simulate triaxial tests, examining the evolution of cohesion and internal friction angle with increasing suction. Both parameters exhibit an upward trend with suction, reflecting the influence of capillary forces and suction-induced densification. Finally, a mathematical model using logarithmic functions is developed to describe the evolution of mechanical parameters as a function of suction, yielding high coefficients of determination ($R^2 > 0.95$) and providing reliable predictive capabilities.

1. Introduction

Water content significantly influences the mechanical behavior of soils. Under unsaturated conditions, capillary forces generated by water at intergranular contacts markedly alter the material's strength and stiffness. While fine-grained soils such as clays experience substantial volumetric changes due to swelling or shrinkage, granular soils like sands develop apparent cohesion through matric suction and capillary bridges (Hornbaker et al., 1997; Wang, Lambert, et al., 2019). In the pendular regime, water forms liquid bridges between grains, producing attractive forces that affect the overall mechanical response.

At the macroscopic level, many constitutive models have been proposed to describe unsaturated soils (Alonso et al., 1990; Gens et al., 2006), but most rely on empirical calibration and do not capture particle-scale mechanisms. In contrast, the Discrete Element Method (DEM) provides a robust framework for simulating granular materials by directly modeling interparticle interactions (Cundall & Strack, 1979), allowing detailed analysis of local force transmission, particle rearrangements, and micromechanical phenomena such as rolling and adhesion.

Several DEM studies have investigated capillary forces at the particle scale in unsaturated soils (Guo, 2014; Soulié, 2006). Wang, Zeng, et al. (2019) extended this work to triaxial test simulations incorporating capillary stresses, and Tran et al. (2020) modeled clayey sludge shrinkage by representing solid and liquid phases as discrete assemblies, showing DEM's versatility for multiphase systems.

A key challenge in DEM modeling of capillary effects is accurately representing adhesion forces as functions of particle size, spacing, and water content. Simplified formulations, such as those by Scholtès et al. (2009) and the Hill contact model (Tan et al., 2014; Potyondy, 2019), allow efficient incorporation of capillary forces at contacts. Experimental studies confirm that increasing matric suction enhances compressive strength, stiffness, and cohesion in compacted soils (Gerard et al., 2015; Bui et al., 2014). The effect on the friction angle depends on soil type, initial density, suction level, and testing protocol. Some

* Corresponding author.
E-mail addresses: anjarasoarico@gmail.com (J. R. Anjarasoaherilalaina)

ISSN 2291-8752 (Online) - ISSN 2291-8744 (Print)

doi: 10.5267/j.esm.2026.2.004

studies indicate that it remains relatively constant with suction (Cai et al., 2024; Wang, Pufahl, et al., 2002; Wheeler & Sivakumar, 2000), while others report an increase (Escario & Sáez, 1986; Lee et al., 2005; Yoshida et al., 1991), or a decrease (Estabragh & Javadi, 2008; Maatouk et al., 1995).

This study models a low-plasticity clayey silt under varying matric suctions to evaluate how suction affects its dimensions, strength, and stiffness. We assume that capillary forces act as adhesion at interparticle contacts, including in the absence of direct contact, and influence macroscopic parameters such as cohesion and internal friction angle through particle rearrangements. PFC3D (Itasca Consulting Group, 2021) treats particles as rigid bodies within granular assemblies. Contacts occur at infinitesimal points, and the contact behavior is "soft," allowing slight overlaps related to the contact force via a force-displacement law. Bonds can also form at contact points. These assumptions enable calibration of mesoscale interaction parameters to reproduce uniaxial compression tests under saturated conditions. The model is then extended to simulate triaxial tests at different suction levels, with key parameters fitted using logarithmic functions of suction.

2. Discrete Element Method

2.1. General Principles

The Discrete Element Method (DEM) highlights the local phenomena observed at the mesoscale of a granular mixture, allowing for a better understanding of the internal structure's evolution under stress (Cundall & Strack, 1979). It models a granular medium by representing it as an assembly of grains. The displacements of these grains or particles are assumed to be those of a rigid body, with deformations presumed to be localized at the contact points. The principle of DEM is based on the successive application of the equation of motion for a rigid body subjected to loads (displacements or forces), followed by the calculation of forces generated by contacts between particles according to the force-displacement law. For each pair of contacting particles, systems of normal and tangential springs (k_n, k_s) as well as dashpots (c_n, c_s) (**Fig. 1a**) are associated with the contact points to determine the contact forces and dissipate energy. The set of contact points between two particles forms a circular surface, representing the intersection between a plane and a sphere at the contact plane, as illustrated in **Fig. 1b.**

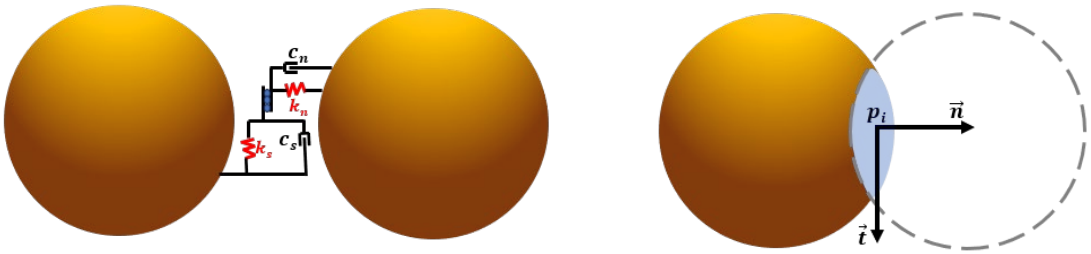

Fig. 1. Basic Principle of Particle Contacts: **(a)** Mechanical Elements; **(b)** Contact Surface.

$\vec{t}$ and $\vec{n}$ represent respectively the tangential vector and the normal vector to the contact surface while p_i is the contact point

2.2. Equation of Motion

According to Cundall & Strack, (1979), the Newton's second law to a particle results in the following equation for acceleration $\ddot{U}$

$$m_e \ddot{U} = F^c + F^d + F^g \quad (1)$$

where $F^c = KU$ is the contact force with K the stiffness matrix including normal and tangential rigidity(k_n, k_s) and U the relative displacement vector between the two particles; $F^d = -c\dot{U}$ is the damping force where $\boldsymbol{c}$ is the damping coefficient and $\dot{U}$ represents the relative velocity between the two particles in contact, $F^g = mg$ is the gravitational force, where g is the gravitational acceleration and $m_e = \frac{m_1 m_2}{m_1 + m_2}$ is the averaged mass of two particles with m_1 and m_2 representing the respective masses of the particles 1 and 2 in contact.

2.3. Contact Models

2.3.1. Linearpbond Model

The Linearpbond contact model is a model based on a linear relationship between force and displacement, implemented in PFC 3D (Particle Flow Code in 3 Dimensions) software (Itasca Consulting Group, 2021). This model is particularly convenient to reproduce macroscopic stiffness because the stiffness parameters at the contact between particles are adjusted through the deformability method to reproduce the deformability of the assembly using an isotropic material model, described

by the elastic constants of Young's modulus ($emod$) and Poisson's ratio (which incorporates the stiffness ratio $kratio$ (Potyondy, 2004). It is often used in modeling the deformability of a homogeneous, isotropic, and well-connected granular assembly experiencing small-strain deformation.

2.3.2. *Hertz Model*

The Hertz contact model is derived from the Mindlin theory (Mindlin & Deresiewicz, 1953). It generates normal and shear forces based on the theoretical analysis of the deformation of smooth, elastic spheres in frictional contact, with a zero-contact moment. The nonlinear Hertz force, denoted F^h, is decomposed into normal forces F_n^h and shear forces F_s^h as follows (Itasca Consulting Group, 2021; Potyondy & Cundall, 2004; Potyondy, 2015).

For normal force:

$$F_n^h = \begin{cases} -h_n |g_c|^{\alpha_{hertz}} & , \ g_c < 0 \\ 0 & , \ otherwise \end{cases} \tag{2}$$

with

$$h_n = \frac{4G\sqrt{\frac{R_1 R_2}{R_1+R_2}}}{3(1-v)} \tag{3}$$

G and v are the effective shear modulus (hz_shear) and poisson's ratio (hz_poiss). R_1 and R_2 are the radii of the contacting particles and g_c is the contact gap.
For shear forces:

$$F_s^h = \begin{cases} F_s^* & , F_s^* \le F_s^\mu \\ \frac{F_s^\mu F_s^*}{\|F_s^*\|} & , otherwise \end{cases} \tag{4}$$

$$F_s^* = (F_s^h)_0 + k_s \Delta\delta_s \tag{5}$$

where

$$k_s = \frac{2(1-v)}{2-v} \alpha_{hertz} h_n^{1/\alpha_{hertz}} (F_n^h)^{(\alpha_{hertz}-1)/\alpha_{hertz}} \tag{6}$$

$(F_s^h)_0$ is the shear force computed at the start of the timestep. $\Delta\delta_s$ is the relative shear displacement increment between the two particles in contact. α_{hertz} is a positive real number with a default value of 1.5. The shear strength is given by:

$$F_s^\mu = \mu F_n^h \tag{7}$$

where μ is the friction coefficient ($fric$).

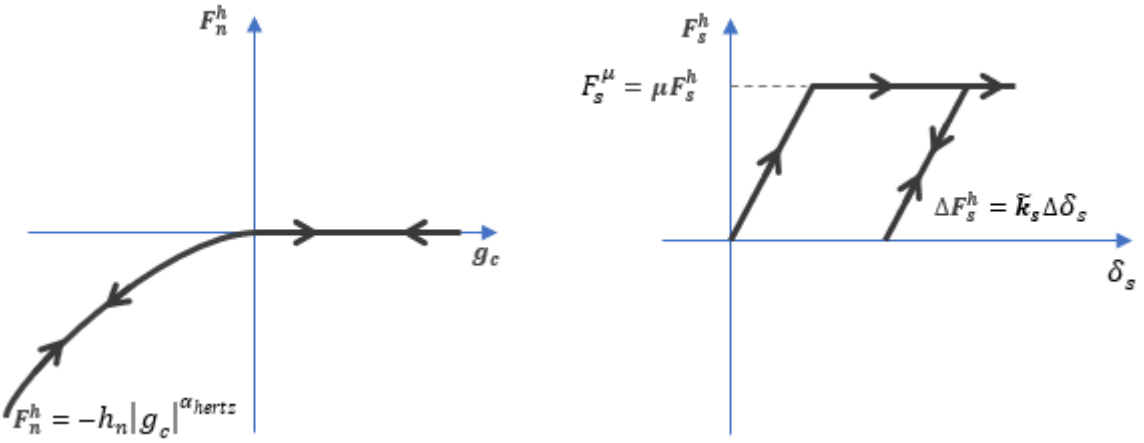

(a) (b)

Fig. 2. Hertz Contact Model:(a) Normal Force vs Contact Gap; (b) Shear Force vs Shear Displacement (Potyondy & Cundall, 2004).

The normal and tangential components of the Hertz contact model indicate that the nonlinear normal force F_n^h is activated only when the interparticle gap g_c is negative, signifying an overlap and effective contact (**Fig. 2a**). The tangential force F_s^h evolves elastically with the tangential displacement δ_s, limited by the Coulomb friction criterion $F_s^\mu = \mu F_n^h$ (**Fig. 2b**).

2.3.3. Hill Model

The Hill contact model, proposed by Tan et al. (2014) and implemented in PFC3D by Potyondy (2019), converts matric suction into intergranular adhesion through the effect of capillary bridges. This model represents capillary attraction by a normal compressive force proportional to suction, which is maximal at grain contact and decreases exponentially until the liquid bridge ruptures. It is therefore partially physically based, as it accounts for the attractive force induced by capillary bridges, but also partially empirical since the moisture-gap parameter must be calibrated to reproduce macroscopic experimental results. The contact is modeled as a nonlinear, frictional, tensionless elastic interface carrying a force $\boldsymbol{F^c}$ with zero moment $\boldsymbol{M^c}$:

$$\boldsymbol{F^c} = \boldsymbol{F^s} + \boldsymbol{F^m} \quad ; \quad \boldsymbol{M^c} \equiv \boldsymbol{0} \tag{8}$$

where F^m is the moisture force and F^s the surface interaction force.

$$\boldsymbol{F^m} = \begin{cases} \psi\pi(R_0)^2 & , g_c < 0 \\ \psi\pi(R_0)^2 \, exp\left(-\dfrac{g_c}{2R_0}\right) & , 0 \le g_c \le 2R_0 \\ 0 & , g_c > 2R_0 \end{cases} \quad ; \quad R_0 = min(R_1, R_2) \tag{9}$$

where g_c is the distance between two particles and R_1, R_2 are the respective radii of the contacting particles. This Hill contact force is represented in **Fig. 3**, as a function of the contact gap.

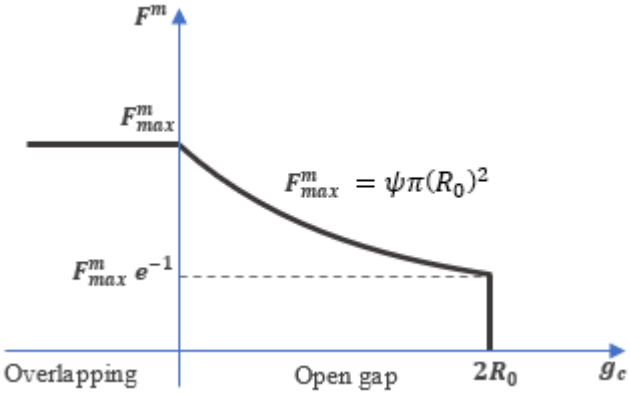

Fig. 3. Moisture Force as a Function of Contact Gap for the Wet Hill Model.

The surface interaction force F^s is decomposed into the Hertzian force F^h and the dashpot force F^d, and can be further divided into normal forces F_n^s and shear forces F_s^s.

For the update of the normal force F_n^s :

$$F_n^s = F_n^h + F_n^d = \begin{cases} -\tilde{k}_n {\delta_0}^{\frac{3}{2}} - \tilde{\eta}_n {\delta_0}^{\frac{1}{4}} \dot{\delta}_0 & , \delta_0 > 0 \\ 0 & , \delta_0 \le 0 \end{cases} \tag{10}$$

where

$$\tilde{k}_n = \frac{4}{3}\left(\frac{E_1 E_2}{E_1(1-v_2^2) + E_2(1-v_1^2)}\right)\sqrt{\frac{R_1 R_2}{R_1 + R_2}} \tag{11}$$

$$\tilde{\eta}_n = \alpha_h \sqrt{m_e \, \tilde{k}_n} \tag{12}$$

$\delta_0 = -g_c$ is the gap between particles, counted positively when overlapping. $\dot{\delta}_0$ is the relative translational velocity normal to the contact plane. $(E_i)_{i=1,2}$ and $(v_i)_{i=1,2}$ are the Young's modulus (*young_mod*) and Poisson ratio (*pois_ratio*) of body i. For shear forces:

$$F_s^s = \begin{cases} F_s^* & ,\delta_0 > 0 \; and \; \|F_s^*\| \le F_s^\mu \\ \dfrac{F_s^\mu F_s^*}{\|F_s^*\|} & ,\delta_0 > 0 \; and \; \|F_s^*\| > F_s^\mu \\ 0 & ,\delta_0 \le 0 \end{cases} \tag{13}$$

$$F_s^* = (F_s^h)_0 - \tilde{k}_s \delta_0^{\frac{1}{2}} \dot{\delta}_s \Delta t - \tilde{\eta}_s \delta_0^{\frac{1}{4}} \dot{\delta}_s \tag{14}$$

where

$$\tilde{k}_s = 8\left(\frac{2(1+v_1)(2-v_1)}{E_1} + \frac{2(1+v_2)(2-v_2)}{E_2}\right)^{-1} \sqrt{\frac{R_1 R_2}{R_1 + R_2}} \tag{15}$$

$$\tilde{\eta}_s = \alpha_h \sqrt{m_e \, \tilde{k}_s} \tag{16}$$

Here, $(F_s^h)_0$ is the shear force computed at the start of the timestep, respectively. $\dot{\delta}_s$ is the relative translational velocity tangentially to the contact plane of the two particles in contact. α_h is the damping constant (*damp_con*). m_e is the averaged mass of the two particles as already defined in the framework of Eq. (1). The shear strength F_s^μ is given in Eq. (7).

3. Simulation Procedure

Based on the DEM and the contact models integrated into PFC3D 6.00.13 developed by ITASCA Consulting Group (22) as well as experimental results from samples subjected to different suctions from Gerald et al. (2015), this study determines the local parameters at the contact level by comparing experimental results with those from simulations. The simulation process is divided into three distinct stages as illustrated in **Fig. 4**.

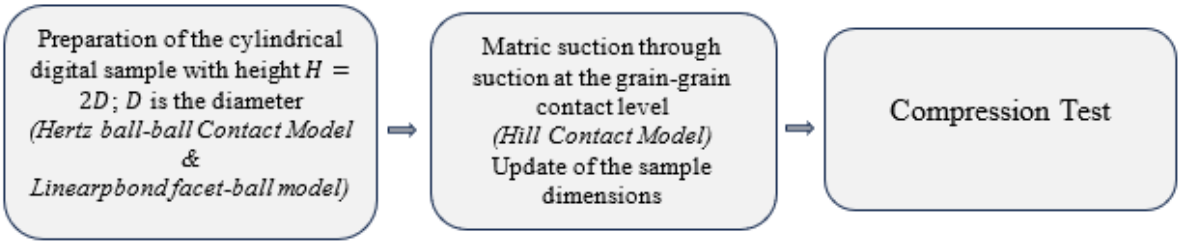

Fig. 4. Schematic Representation of the three Main Simulation Stages: (i) Preparation of the Cylindrical Digital Sample, (ii) Application of Matric Suction at the Grain–Grain Contact Level with Dimension Update, and (iii) Subsequent Compression Test.

3.1. Digital Sample Preparation

The digital sample considered in this work consists of numerically modeled spherical grains representing a low-plasticity clayey silt, with 13% of particles having a diameter of 176 µm, 64% between 176 µm and 200 µm, and 23% between 200 µm and 360 µm. The grain size distribution of the virtual sample is illustrated in **Fig. 5.**

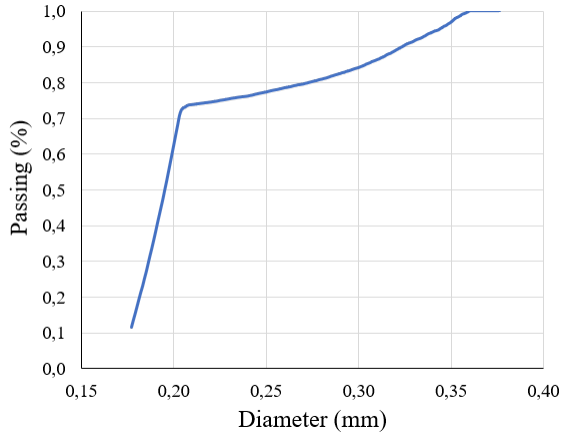

Fig. 5. Cumulative Particle Size Distribution of the Digital Sample

The sample dimensions are 7.2 mm in height (H) and 3.6 mm in diameter (D), chosen so that the maximum grain diameter does not exceed one-tenth of the sample diameter. The digital sample has an initial porosity of 0.28, reflecting its packing configuration. The sample is assembled by placing spherical grains differentiated only by their size and solid particle density into a cylindrical container confined between two rigid plates separated by the height H. Particles with diameters between 176 µm and 200 µm have a solid particle density of 1.75 g/cm³, while those with diameters between 200 µm and 360 µm have a density of 2.65 g/cm³.

3.2. Application of Suction Force

Under the effect of the capillary force F^m, the sample undergoes compression. As illustrated in **Fig. 6,** the opposing displacement of the two plates allows for the measurement of the sample's new height, while the compression of the cylindrical container is used to determine the updated radius, until positive axial stress is achieved on the plates and positive radial stress on the container.

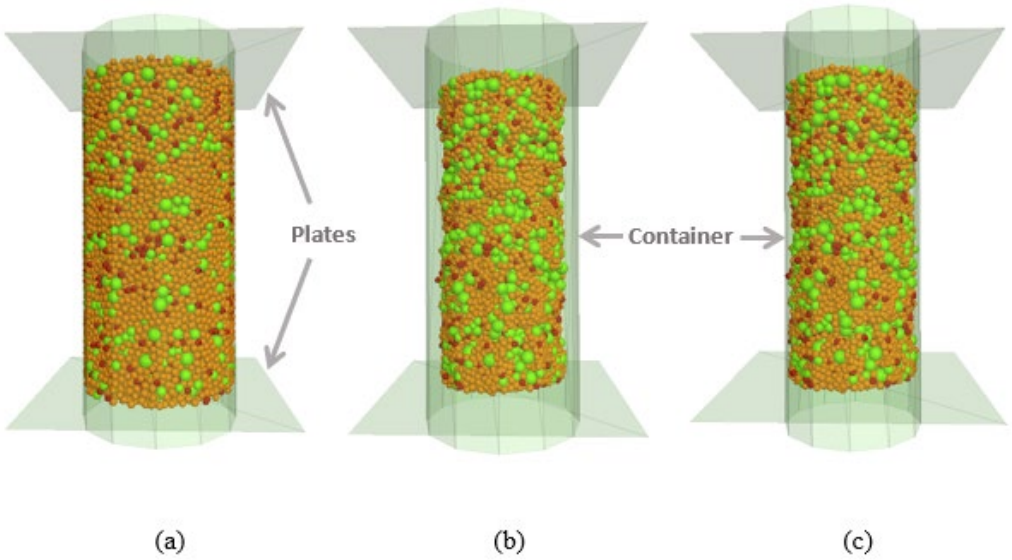

Fig. 6. Digital Sample at Different Stages: (a) before Suction Application, (b) after Suction Application, and (c) after Suction Application with Updated Dimensions.

The volumetric strain, denoted by $\boldsymbol{\varepsilon_v}$, is defined by the relation $\varepsilon_v = \frac{\Delta V}{V}$, where ΔV represents the difference between the initial volume V of the sample and the final volume after the application of suction. **Fig. 7** shows the evolution of volumetric strain as a function of the level of applied suction. It is observed that there is a significant shrinkage of the assembly for low levels of suction (< 10 MPa) while the volume remain globally constant for further suction increases (> 10 MPa).

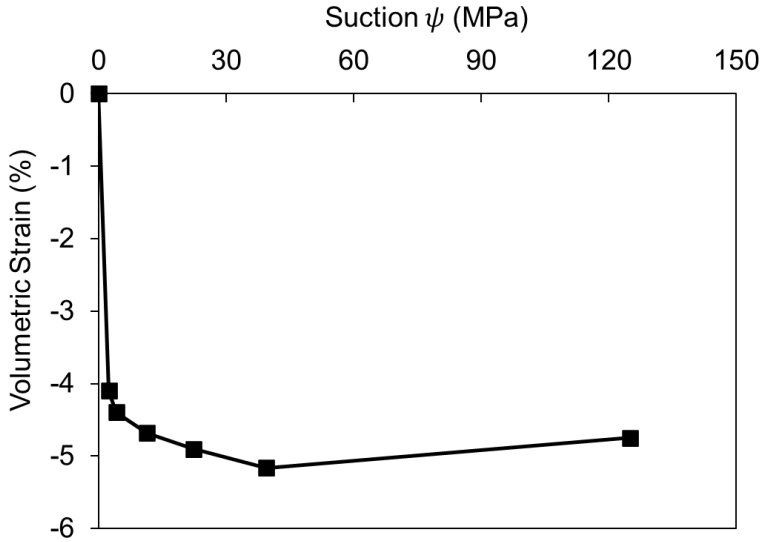

Fig. 7. Volumetric Strain as a Function of Suction ψ.

3.3. Uniaxial Compression Tests

This section presents the modeling of the sample's compressive strength to evaluate its resistance and stiffness, with numerical results benchmarked against the experimental data of Gerald et al. (2015). Silty soil specimens were compacted to a dry unit weight of 2000 kg/m³ at 8% initial water content, then conditioned under controlled relative humidity to impose matric suctions from 4.17 MPa to 125 MPa before uniaxial compression. Additional tests were performed on specimens in as-compacted and fully re-saturated states.

In the DEM simulations conducted with PFC3D, the uniaxial compression test is reproduced by removing the cylindrical container, whereas the triaxial tests are performed under isotropic confining pressure applied via a finite element structure replacing the container. The top and bottom platens are then displaced vertically in opposite directions at a prescribed velocity v, and the stress-strain curve is obtained from the (ε, q) data pairs:

$$\varepsilon = \frac{[H - (Z_s - Z_i)]}{H} \tag{17}$$

$$q = \frac{0{,}5\left(f_{c_s} + f_{c_i}\right)}{\pi R^2} \tag{18}$$

with Z_s and Z_i being the position of the top and bottom platens on the vertical axis, respectively. f_{c_s}, f_{c_i} are the forces exerted respectively by the top and bottom platens on the sample and R is the radius of the cylindrical specimen.

4. Numerical Results of Uniaxial Tests

4.1. Parameters Calibration and Results of Uniaxial Compression Simulations

To identify the optimal local parameters for the Discrete Element Method, the contact model parameters (Hertz and Hill) were systematically varied, and the resulting stress-strain curves were compared with experimental data. The displacement rate of the top and bottom platens was fixed at 0.02 %/min, in accordance with Cheng et al. (2024). The selected local parameters for the contact model are summarized in **Table 1**.

Table 1. Local Parameters Selected for the Contact Model

Stage of simulation	Contact type	Contact model	Parameter	Value
Sample preparation	ball-ball	Hertz model	*hz_shear,* *hz_poiss,* *fric*	1.40E+07 Pa - 0.32 0.32
Suction application and compression	ball-ball	Hill model	*Suction* *damp_con* g_m *young_mod* *pois_ratio*	ψ 0.1 1.60E-4 m 3.50E+08 Pa - 0.32

Calibration showed that *hz_shear* predominantly governs the peak material strength, whereas *hz_poiss* and *fric* have a minor influence in the Hertz model. Regarding suction, the contact parameter *make_wet_gap* (g_m) and the grain Young's modulus (*young_mod*) play a significant role. Both *young_mod* and the Poisson ratio (*pois_ratio*) strongly affect the material behavior under high suction conditions. The initial platen positions, their displacement rate, and the contact stiffness influence the stress-strain response near the origin as well as around the peak stress.

The comparison of experimental results with DEM simulations across suction levels from 0 to 125 MPa (**Fig. 8**) demonstrates that the model accurately captures both the initial slope and the peak stress. Post-peak strength reduction is slightly more gradual than observed experimentally, particularly for ψ = 2.47, 22.29 and 39.46 MPa. At low suction (ψ = 0 MPa), the failure strain is slightly overestimated, whereas at high suction (ψ = 125 MPa), simulation and experimental results are in excellent agreement.

4.2. Analysis and Comparison

This section compares the simulation results with experimental measurements in terms of uniaxial compressive strength (**Fig. 9**) and stiffness modulus (**Fig. 11**) under different applied suctions.

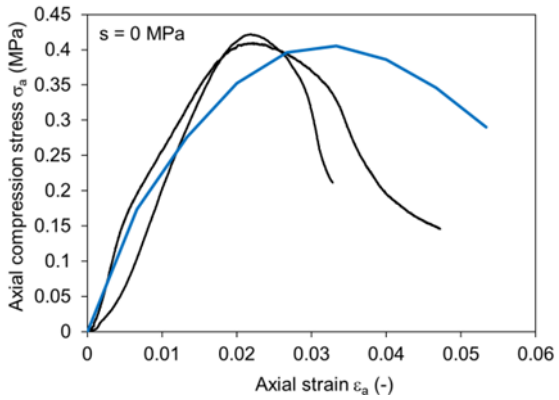

(a)

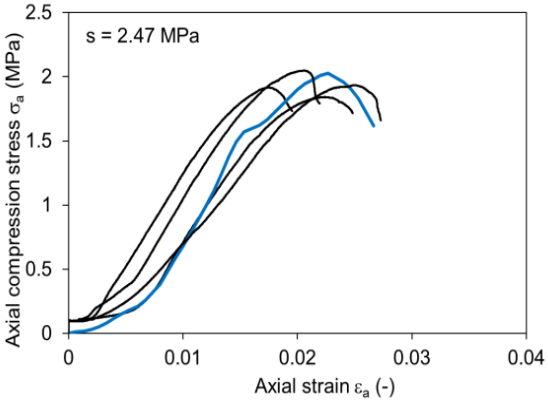

(b)

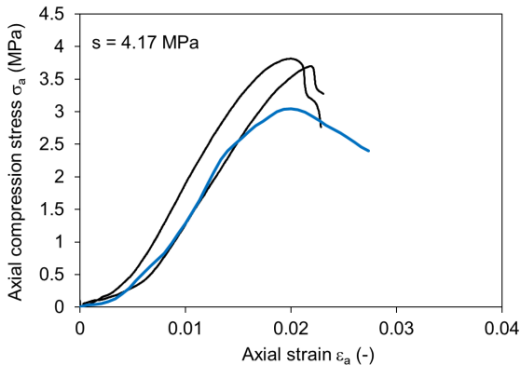

(c)

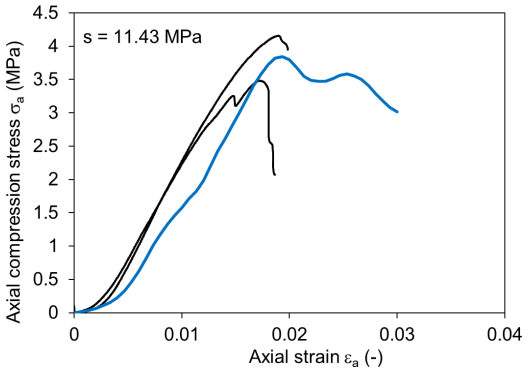

(d)

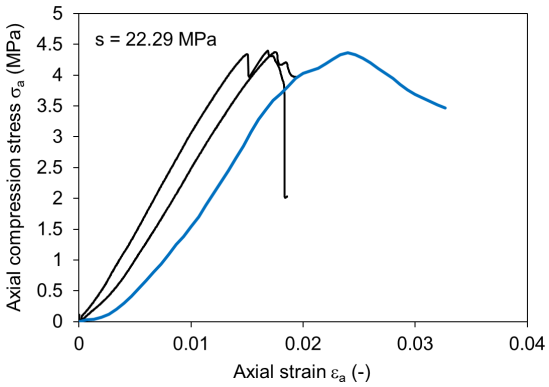

(e)

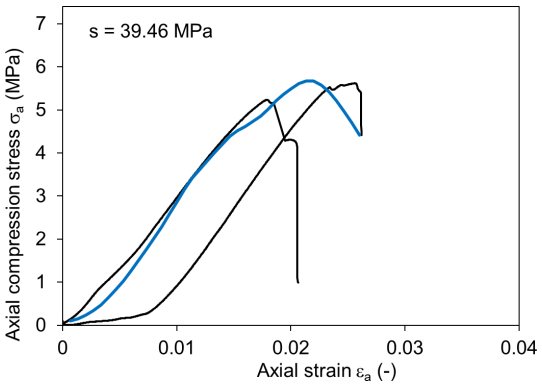

(f)

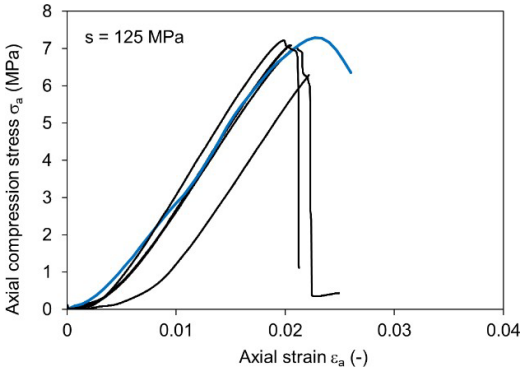

(g)

Fig. 8. Experimental Results and Simulations for Different Suction Values: (a) $\psi = 0MPa$; (b) $\psi = 2.4MPa$; (c) $\psi = 4.17MPa$; (d) $\psi = 11.43MPa$; (e) $\psi = 22.29MPa$; (f) $\psi = 39.46MPa$; (g) $\psi = 125MPa$. Blue Curve: Simulations. Black Curve: Experiments.

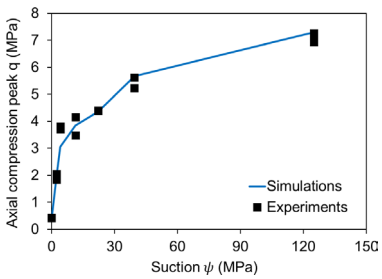

Fig. 9. Uniaxial Compressive Strength versus Imposed Suction. Blue Curve: Simulations; Scatter Plot: Experiments.

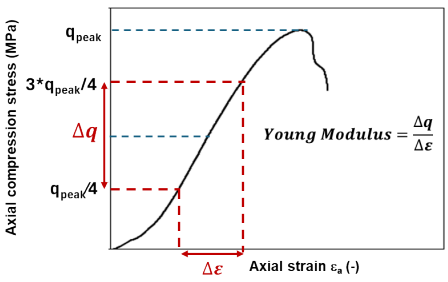

Fig. 10. Illustration of the method for calculating Young's modulus

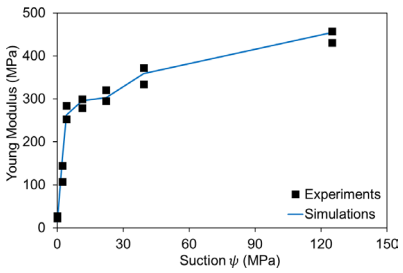

Fig. 11. Young Modulus as a Function of Imposed Suction. Blue Curve: Simulations. Scatter Plot: Experiments.

A chi-square test based on 7 observations yields:

$$\chi^2_{calc} = 0{,}181 < \chi^2_{(0.02\,;6)} = 15.033 \tag{19}$$

indicating statistical compatibility between simulations and experiments at the 98% confidence level.

The Young modulus is obtained as the slope of the axial stress (q) – axial strain (ε) curve in a zone located between $q_{peak}/4$ and $3q_{peak}/4$, where q_{peak} is the uniaxial compressive strength, as illustrated in **Fig. 10.** For this parameter, the chi-square test gives:

$$\chi^2_{calc} = 0{,}144 < \chi^2_{(0.02\,;6)} = 15.033 \tag{20}$$

confirming the statistical compatibility of the data at the 98% confidence level.

5. Effect of Suction on Strength Parameters

5.1. Extension to Triaxial Compression Simulations

To deepen the study and better understand the influence of matric suction forces applied to soil, we extended the numerical modelling to triaxial compression tests in order to determine friction angle and cohesion as a function of suction. Here the results will be analyzed in net stress such that the strength parameters (cohesion and friction angle) are expected to change as a function of suction (Fredlund, 2006). The approach used for the triaxial tests at this stage follows the same procedure as the uniaxial compression test described in the previous Section 3.3. However, before proceeding with the compression, we first apply an isotropic confinement stress σ_3 using a servo-mechanical system, which exerts this stress uniformly on the sample in all directions. To this end, we propose to simulate various triaxial compression tests under different confining pressures (0, 200, 300 and 400 kPa) for the same various suctions than the uniaxial compression tests simulated previously, and present the stress state at failure on the $p-q$ plot to measure these strength parameters as a function of applied suction variations. In this case, the Mohr-Coulomb failure criterion for the soil will be represented by the line $q_{max} = Mp + k$ that connects the (p, q_{max}) pairs obtained, where $p = (\sigma_1 + 2\sigma_3)/3$ represents the mean effective stress and $q_{max} = \sigma_1 - \sigma_3$ represents the deviatoric stress at failure. σ_1 is the axial stress at failure while σ_3 is the confining pressure. Based on the modelling results, we calculate the corresponding values of p_i and $q_{\max_i}$ for each confining pressure σ_3, and $q_{\max_i}$ is be the maximum stress at failure on the resulting stress-strain curve. Subsequently, using the least squares method, we determine the trend line of the q_{max} line with the following system of equations:

$$\begin{cases} M\sum_{i=1}^{n} p_i^2 + k\sum_{i=1}^{n} p_i = \sum_{i=1}^{n} q_{max_i}\, p_i \\ M\sum_{i=1}^{n} p_i + kn = \sum_{i=1}^{n} q_{max_i} \end{cases} \tag{21}$$

where n is the number of tests conducted.

Using the obtained values of M and k, we can determine the cohesion c and friction angle φ:

$$\varphi = Arcsin\left(\frac{3M}{6+M}\right) \;,\; c = k\frac{tan\varphi}{M} \tag{22}$$

5.2. Numerical Results of Triaxial Tests

Fig. 12 represents the simulation results of triaxial compression tests under the applied confinement stresses of $\sigma_3 =$ 0 ,200 ,300 and 400 kPa and the 7 suction levels.

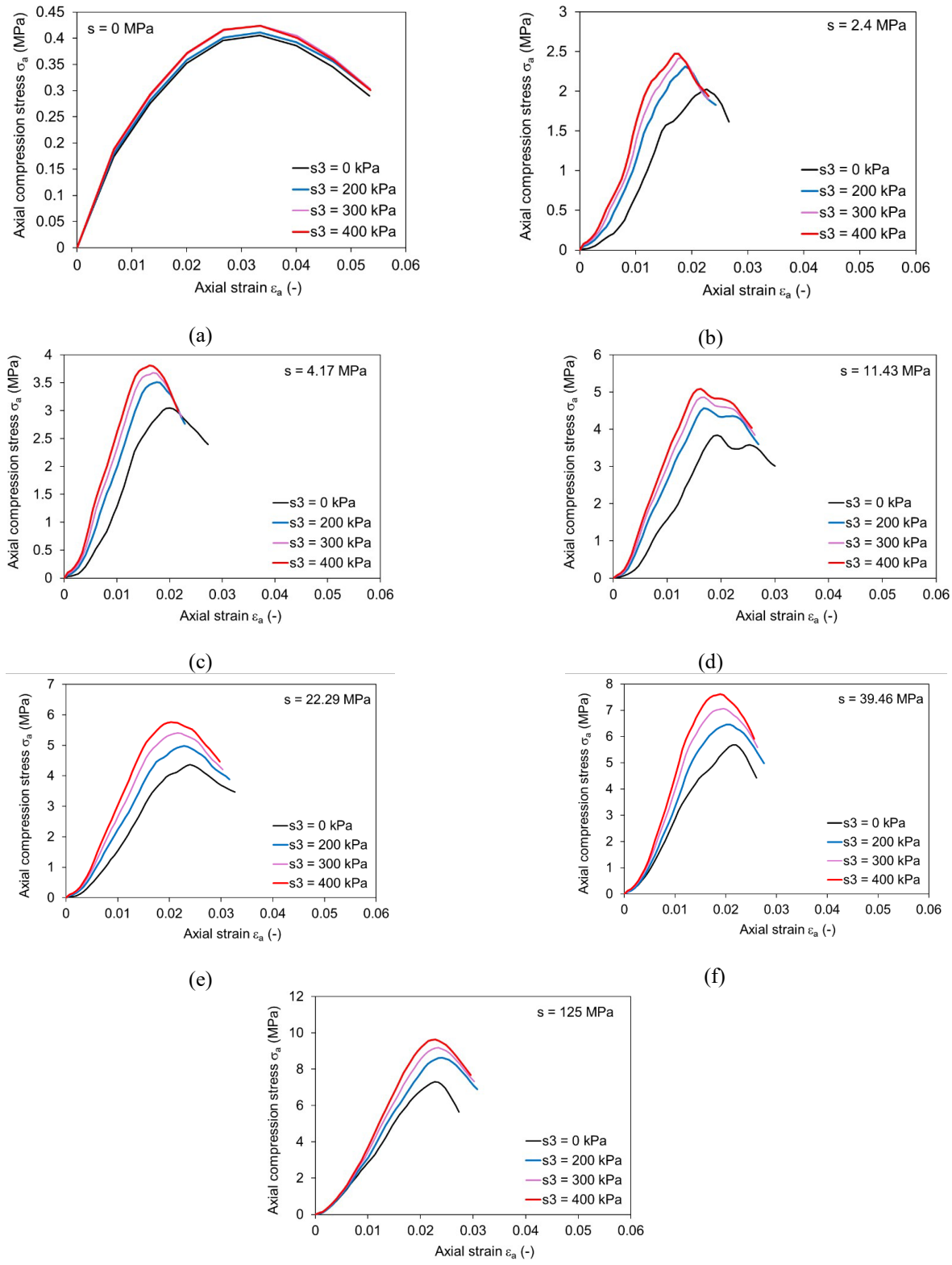

Fig. 12. Stress-Strain Curves for the Sample under Triaxial Compression Tests at Various Confining Pressures and Suctions: (a) $\psi = 0MPa$ Saturated Conditions; (b) $\psi = 2.4MPa$; (c) $\psi = 4.17MPa$; (d) $\psi = 11.43MPa$; (e) $\psi = 22.29MPa$; (f) $\psi = 39.46MPa$; (g) $\psi = 125MPa$.

Note that the case of zero confining stress ($\sigma_3 = 0\ kPa$) corresponds to the modelling results of uniaxial compression tests, used to calibrate the parameters. It is observed that both confining stress and suction induces an increase of strength and stiffness.

5.3. Evaluation of Shear Strength Parameters

Shear strength parameters of the numerical sample were evaluated under confining pressures of 0, 200, 300, and 400 kPa and varying suction levels. The stress state at failure (**Fig. 13**) follows the Mohr-Coulomb criterion, with scatter points representing individual failure stresses and a trend line indicating the overall failure envelope, while the predicted friction angle and cohesion across suction levels are shown in **Fig. 14.** These results are specific to the applied confining conditions and may not directly extend to other confinement setups or samples with different grain size distributions. In addition, the estimated friction angle and cohesion are influenced by the selected contact model and calibration parameters.

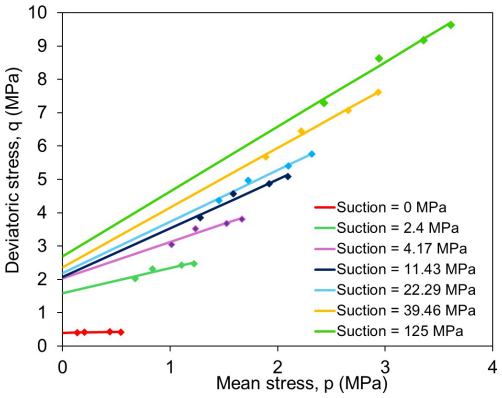

Fig. 13. Failure Line Based on the Mohr-Coulomb Criterion: Scatter Plot of Failure Stresses with Trend Line.

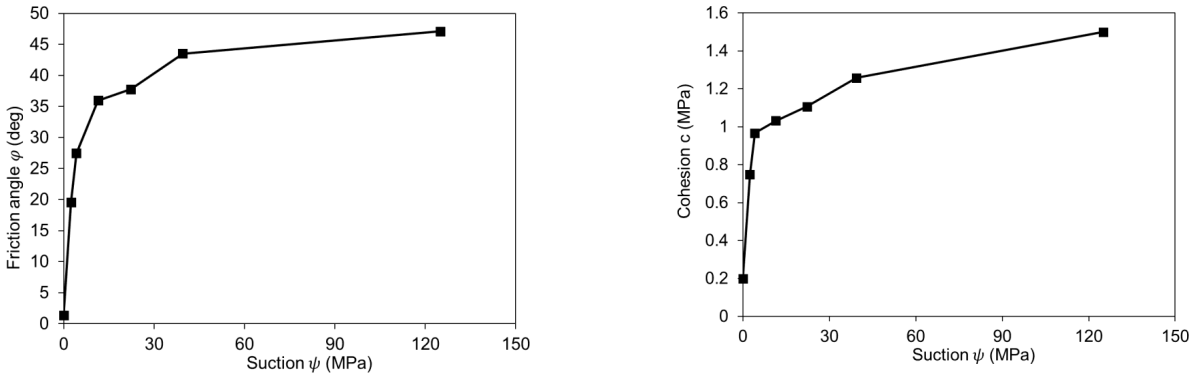

(a) (b)

Fig. 14. Friction Angle (a) and Cohesion (b) of the Sample at Different Suctions, Predicted by Simulations.

6. Mathematical Model

The analysis of the simulation curves (**Fig. 9, Fig. 11** and **Fig. 14**) shows that the studied mechanical parameters (compressive strength, Young's modulus, internal friction angle, and cohesion) increase rapidly and then approach an asymptotic value. This behavior is well represented by the logarithmic function:

$$\hat{y} = aln(b\psi + 1) \tag{23}$$

The coefficients a and b are determined using the nonlinear least squares method with the Levenberg–Marquardt algorithm. The fitted models for each mechanical parameter as a function of matric suction ψ, along with the determination coefficients R^2, are summarized in **Table 2**.

Table 2. Logarithmic Models Fitted to Relate Mechanical Parameters to Matric Suction ψ

Mechanical Parameter	Fitted Model	R^2
Maximum Compressive Strength q_{max}	$q_{max} = 1{,}3671 * ln\ (1{,}4746 * \psi + 1)$	0,98
Young's Modulus E	$E = 64.9014 * ln\ (7.2014 * \psi + 1)$	0,97
Friction Angle φ	$\varphi = 6.8448 * ln\ (11.1439 * \psi + 1)$	0,98
Cohesion c	$c = 0.1726 * ln\ (38.6825 * \psi + 1)$	0,95

As shown in **Table 2,** the logarithmic models accurately capture the evolution of the mechanical parameters with matric suction, with high determination coefficients.

7. Discussion

This study demonstrated that suction significantly influences the shear strength parameters of partially saturated granular materials, namely cohesion and internal friction angle. The DEM simulations conducted here allow for a detailed analysis of these effects and provide insight into the local mechanisms governing mechanical behavior under varying suction conditions.

The results show that cohesion increases with suction, primarily due to the capillary cohesion effect captured by the Hill contact model, which reproduces capillary forces between particles generated by liquid bridges. The increase in friction angle with suction is less commonly reported in the literature. In this study, it can be attributed to the densification of the material induced by suction application (**Fig. 7**). This densification brings particles closer together, creates new contacts, and reduces interparticle gaps, allowing the Hill model to generate additional wet contacts. Consequently, the increase in friction angle with suction (**Fig. 14a**) follows the same trend as the volumetric contraction induced by suction. The effect is particularly pronounced at low suction values (< 10 MPa), while it becomes almost negligible at higher levels (> 10 MPa). Suction therefore plays a dual role in strengthening the material: it enhances capillary forces and induces densification that promotes new contacts, thereby increasing overall material strength.

These observations are consistent with the findings of Alsherif and McCartney (2014), who reported that the larger peak friction angles observed in unsaturated silt samples at high suction could be due to the substantial reduction in initial void ratio before shearing, induced by the application of high suction. More broadly, the literature does not provide a consistent trend for the evolution of friction angle with suction; it may increase, decrease, or remain constant depending on soil type, initial relative density, suction level, and the methods used for sample preparation, suction application, and consolidation. Nevertheless, the numerical predictions obtained here align with the results of Yoshida et al., (1991)**,** who observed an increase in friction angle from approximately 20° to 40° as the degree of saturation decreased from 100% to 30% in silty sands.

The findings highlight the effectiveness of coupling the Hertz and Hill models in PFC3D to capture suction effects on cohesion and friction angle, while linking these effects to local physical mechanisms such as densification and capillary forces. It should be noted, however, that these conclusions depend on the applied confinement conditions and calibration parameters, and their extrapolation to other configurations or soils with different particle size distributions should be approached with caution. The simplified spherical particle geometry used in the simulations also represents a limitation. Thus, suction simultaneously affects both cohesion and internal friction angle, reinforcing the material through complementary mechanisms.

8. Conclusion

Understanding the mechanical behavior of partially saturated granular materials is crucial in geotechnical and environmental engineering, as suction significantly affects their strength and deformation properties. This study demonstrates the effectiveness of the Discrete Element Method (DEM) for modeling the influence of suction on these materials. In PFC3D, the Hertz contact model was coupled with the Hill model, whose force is proportional to suction and decays exponentially with interparticle distance, thereby capturing capillary effects. After calibrating the parameters of both contact models, the simulations successfully reproduced the stress–strain curves observed in uniaxial compression tests at various suction levels, accurately reflecting the evolution of strength and stiffness. The modeling was subsequently extended to triaxial simulations to assess the influence of suction on key mechanical parameters such as cohesion and internal friction angle. A functional modeling approach was employed to develop a predictive logarithmic model of the form $\hat{y} = aln(b\psi + 1)$, which showed excellent agreement with the simulated results ($R^2 > 0.95$), providing a practical tool for rapidly estimating mechanical parameters as a function of suction for this type of soil. For future work, it would be relevant to validate these findings through experimental triaxial tests and to enhance the numerical models by incorporating more realistic particle shapes and advanced formulations, in order to better capture the complexity of soil behavior.

9. Competing Interests

The authors have no competing interests to declare that are relevant to the content of this article. All authors certify that they have no affiliations with or involvement in any organization or entity with any financial interest or non-financial interest in the subject matter or materials discussed in this manuscript.

Author Contributions

José Rico Anjarasoaherilalaina: Methodology, Investigation, Original draft preparation, Writing; **Bertrand François:** Visualization, Supervision, Writing, Validation, Reviewing and Editing; **Luc Rakotondrajaona:** Conceptualization, Supervision

References

Alonso, E. E., Gens, A., & Josa, A. (1990). A constitutive model for partially saturated soils. Géotechnique, 40(3), 405–430.

Alsherif, N. A., & McCartney, J. S. (2014). Effective stress in unsaturated silt at low degrees of saturation. *Vadose Zone Journal, 13*(5), 1–13.

Bui, Q. B., Morel, J. C., Hans, S., & Walker, P. (2014). Effect of moisture content on the mechanical characteristics of rammed earth. *Construction and Building Materials, 54*, 163–169.

Cai, G., Han, B., Asreazad, S., Liu, C., Zhou, A., Li, J., & Zhao, C. (2024). Experimental study on critical state behaviour of unsaturated silty sand under constant matric suctions. *Géotechnique, 74*(5), 409–430.

Cheng, Z., Wang, J., Xu, D. S., & Fan, X. (2024). DEM study on the micromechanical behaviour of sand-clay mixtures. *Powder Technology, 435*, 119400.

Cundall, P. A., & Strack, O. D. L. (1979). A discrete numerical model for granular assemblies. Géotechnique, 29(1), 47–65.

Escario, V., & Sáez, J. (1986). The shear strength of partly saturated soils. *Géotechnique, 36*(3), 453–456.

Estabragh, A. R., & Javadi, A. A. (2008). Critical state for overconsolidated unsaturated silty soil. *Canadian Geotechnical Journal, 45*(3), 408–420.

Fredlund, D. G. (2006). Unsaturated soil mechanics in engineering practice. *Journal of Geotechnical and Geoenvironmental Engineering, 132*(3), 286–321.

Gens, A., Sánchez, M., & Sheng, D. (2006). On constitutive modelling of unsaturated soils. *Acta Geotechnica, 1*(3), 137–147.

Gerard, P., Mahdad, M., Robert McCormack, A., & François, B. (2015). A unified failure criterion for unstabilized rammed earth materials upon varying relative humidity conditions. *Construction and Building Materials, 95*, 437–447.

Guo, P. (2014). Coupled effects of capillary suction and fabric on the strength of moist granular materials. *Acta Mechanica, 225*(8), 2261–2275.

Hornbaker, D. J., Albert, R., Albert, I., Barabási, A. L., & Schiffer, P. (1997). What keeps sandcastles standing? *Nature, 387*(6635), 765–766.

Itasca Consulting Group. (2021). Particle Flow Code, Ver. 7.0 [Computer software]. Itasca. https://docs.itascacg.com/

Lee, I. M., Sung, S. G., & Cho, G. C. (2005). Effect of stress state on the unsaturated shear strength of a weathered granite. *Canadian Geotechnical Journal, 42*(2), 624–631.

Ma, Z., Lu, K., Song, D., Liu, W., Wang, Y., & Li, S. (2023). Study on compaction characteristics and compaction process of an unsaturated silt based on PFC3D. *Applied Sciences, 13*(9), 5547.

Maatouk, A., Leroueil, S., & La Rochelle, P. (1995). Yielding and critical state of a collapsible unsaturated silty soil. *Géotechnique, 45*(3), 465–477.

Mindlin, R. D., & Deresiewicz, H. (1953). Elastic spheres in contact under varying oblique forces. *Journal of Applied Mechanics, 20*(3), 327–344.

Potyondy, D. O. (2015). The bonded-particle model as a tool for rock mechanics research and application: Current trends and future directions. *Geosystem Engineering, 18*(1), 1–28.

Potyondy, D. O. (2019). Hill Contact Model [version 4] (Technical Memorandum ICG7795-L). Itasca Consulting Group, Inc. https://itasca-software.s3.amazonaws.com/udm-library/HillContactModelAug29_2019.pdf

Potyondy, D. O., & Cundall, P. A. (2004). A bonded-particle model for rock. *International Journal of Rock Mechanics and Mining Sciences, 41*(8), 1329–1364.

Scholtès, L., Hicher, P. Y., Nicot, F., Chareyre, B., & Darve, F. (2009). On the capillary stress tensor in wet granular materials. *International Journal for Numerical and Analytical Methods in Geomechanics, 33*(10), 1289–1313.

Soulié, F. (2006). Etude micromécanique de la cohésion par capillarité dans les milieux granulaires humides [Doctoral dissertation]. Montpellier 2.

Tan, D. S., Khazanovich, L., Siekmeier, J., & Hill, K. M. (2014). Discrete element modeling of effect of moisture and fine particles in lightweight deflectometer test. *Transportation Research Record: Journal of the Transportation Research Board, 2433*(1), 58–67.

Tran, K. M., Bui, H. H., Sánchez, M., & Kodikara, J. (2020). A DEM approach to study desiccation processes in slurry soils. *Computers and Geotechnics, 120*, 103448.

Wang, J. P., Lambert, P., De Kock, T., Cnudde, V., & François, B. (2019). Investigation of the effect of specific interfacial area on strength of unsaturated granular materials by X-ray tomography. *Acta Geotechnica, 14*(5), 1545–1559.

Wang, J. P., Zeng, G. H., & Yu, H. S. (2019). A DEM investigation of water-bridged granular materials at the critical state. *Computational Particle Mechanics, 6*(4), 637–655.

Wang, Q., Pufahl, D. E., & Fredlund, D. G. (2002). A study of critical state on an unsaturated silty soil. *Canadian Geotechnical Journal, 39*(1), 213–218.

Wheeler, S. J., & Sivakumar, V. (2000). Influence of compaction procedure on the mechanical behaviour of an unsaturated compacted clay. Part 2: Shearing and constitutive modelling. *Géotechnique, 50*(4), 369–376.

Yoshida, Y., Kuwano, J., & Kuwano, R. (1991). Effects of saturation on shear strength of soils. *Soils and Foundations, 31*(1), 181–186.